Journal of Magnetism and Magnetic Materials 634 (2025) 173555

Contents lists available at ScienceDirect

Journal of Magnetism and Magnetic Materials

journal homepage: www.elsevier.com/locate/jmmm

Research article

Influence of thickness on magnetic properties of RF-sputtered amorphous CoNbZr thin films

Indujan Sivanesarajah [a,*], Leon Abelmann [b], Uwe Hartmann [a]

[a] Institute of Experimental Physics, Saarland University, D-66041 Saarbrücken, Germany
[b] Department of Microelectronics, Delft University of Technology, 2600 AA Delft, The Netherlands

ARTICLE INFO

Keywords:
Amorphous CoNbZr
Thickness dependency
Domain wall transition

ABSTRACT

Amorphous sputtered Co-based thin films are widely used as soft magnetic materials in applications such as sensors, inductors and magnetic flux concentrators. The magnetic properties of these films can be controlled by deposition parameters like film thickness, argon pressure, deposition rate and others. In this study, we present a detailed investigation of the magnetic properties of RF-sputtered $Co_{90}Nb_8Zr_2$ films with thicknesses ranging from 52 nm to 1040 nm. These amorphous films exhibit an average saturation magnetisation of (1.01 ± 0.04) MA/m. As the film thickness increases, there is a significant decrease in coercivity, remanent-to-saturation magnetisation ratio M_r/M_s, and maximum permeability. The change in macroscopic magnetic properties is also reflected by the domain structure. At a thickness of 52 nm, the remanent domain state shows irregular domains, while films thicknesses above 208 nm exhibit flux-closure domain structures instead. The thickness-dependent modifications are attributed to the transition between Néel and Bloch type domain walls, which is expected to occur at approximately 84 nm.

1. Introduction

Amorphous alloys have gained substantial prominence as soft magnetic materials [1–4]. Their lack of long-range atomic order leads to low coercivity and high permeability [1], making them ideally suited for a wide range of applications, including magnetic sensors [5–7], integrated inductors [8–11], and electric motors [12–14]. A deeper understanding of the magnetisation processes and domain structures in such materials is provided by the seminal work of Hubert and Schäfer, which offers both theoretical and experimental perspectives on magnetic domains [15].

Among the various amorphous Co-based alloys, CoNbZr has attracted particular attention due to its high susceptibility, large saturation magnetisation, and low coercive field [16,17]. These properties make it a promising candidate for integrated magnetic flux concentrators and planar thin-film sensors, establishing it as a material of central importance in this field [18–20]. Several studies by Japanese research groups have further investigated the potential of CoNbZr for high-frequency sensor applications and microwave absorption structures [21]. They show that the characteristic impedance increases with increasing film thickness [22], and demonstrated high sensitivity allowing for unshielded magnetocardiogram measurements [23].

CoNbZr films are typically fabricated by sputter deposition. Their magnetic properties are highly sensitive to the Argon sputter pressure. Peng et al. showed that an increase in sputter pressure can cause columnar growth, thereby inducing perpendicular magnetic anisotropy [24]. Similarly, Takahashi et al. showed that an increase in sputter pressure leads to an increase in coercivity [25].

Film thickness plays a pivotal role in determining the magnetic performance of CoNbZr films. Experimental studies have reported an inverse relationship between thickness and coercive field [25–27], as well as an increase in the anisotropy field with increasing thickness [28]. Thick CoNbZr films also tend to develop in-plane uniaxial magnetic anisotropy [27].

Such thickness-dependent effects are not unique to CoNbZr but are also characteristic of other soft magnetic thin films such as CoFeB and NiFe (Permalloy). For example, García et al. [29] reported changes in coercivity, remanence, and domain structure in CoFeB films as a function of induced anisotropy. Similarly, studies on Permalloy films revealed stripe domain formation and a transition into a “transcritical” state near a critical thickness, accompanied by marked changes in coercivity and permeability [30–32]. These parallels underline the general role of deposition conditions, stress, morphology, and dimensionality in shaping the magnetic behaviour of sputtered soft magnetic thin films.

While the fundamental transition from Néel to Bloch domain walls with increasing film thickness is well established in micromagnetic

* Corresponding author.
E-mail address: sivanesa@outlook.de (I. Sivanesarajah).

https://doi.org/10.1016/j.jmmm.2025.173555
Received 12 May 2025; Received in revised form 17 September 2025; Accepted 26 September 2025
Available online 7 October 2025

theory [15], quantitative studies linking this transition to macroscopic magnetic parameters such as permeability and coercivity in amorphous Co-based films remain scarce.

This study addresses this gap by systematically analysing the thickness-dependent magnetic properties of sputtered CoNbZr thin films. Special emphasis is placed on correlating the evolution of domain structures with macroscopic magnetic behaviour, thereby providing insights directly relevant for the optimisation of CoNbZr-based magnetic sensors.

2. Materials and methods

This section describes the fabrication of CoNbZr thin films and the methods used for their structural and magnetic characterisation.

2.1. Sample preparation

CoNbZr films were deposited on Si–SiO_2 substrates of 8 mm × 8 mm, mounted on a rotating holder using magnetron sputtering with a radio frequency (RF) power supply. The target composition of $Co_{85}Nb_{12}Zr_3$ (at. %) was chosen due to the nearly zero magnetostriction ($\lambda_s < 10^{-6}$) [33]. The target-to-substrate distance was set to 12 cm. After reaching a base pressure below $1 \cdot 10^{-8}$ mbar, the films were deposited at an argon pressure of $1.7 \cdot 10^{-3}$ mbar using an RF power of 100 W applied to the magnetron target. The deposition was deliberately carried out at the lowest stable sputtering pressure of the system in order to avoid the columnar growth and coercivity increase observed at elevated argon pressures [24,25]. The deposition rate of (4.9 ± 0.2) nm/min was determined by cross-sectional TEM analysis of a reference film sputtered for 60 min. By adjusting the sputtering time, films with thicknesses between 52 nm and 1040 nm were fabricated. This thickness range was chosen in accordance with previous studies [34–36].

For magnetic domain structure analysis via magnetic force microscopy (MFM), CoNbZr films were patterned into 20 µm × 20 µm squares using a FEI Helios NanoLab 600 focused ion beam (FIB) at an acceleration voltage of 30 kV. Initially, an outer frame was patterned to coarsely remove material at a beam current of 21 nA, followed by patterning of the final structures at a current of 6.5 nA. No ion beam imaging was performed of the patterned area to prevent detrimental effects of Ga ions on the magnetic properties of the structures [37].

2.2. Microstructural characterisation

X-ray diffraction (XRD) patterns of the investigated samples were recorded at room temperature using a Bruker D8-A25-Advance diffractometer in Bragg–Brentano $\theta - \theta$ geometry, with a goniometer radius of 280 nm and Cu K_α radiation (λ = 154.0596 pm). A 12 µm Ni foil served as a K_β filter and a variable divergence slit was positioned at the primary beam side. A Bruker LYNXEYE detector with 192 channels was employed on the secondary beam side. Experiments were conducted in a 2θ range of 30° to 60° with a step size of 0.013° and a total scan period of 4 h.

Electron diffraction patterns were acquired using a JEOL 2011 transmission electron microscope (TEM), equipped with a LaB_6 cathode and operated at 200 kV. TEM slices were prepared by milling a 15 µm × 5 µm area from the continuous film using FIB followed by in situ lift-out with a micromanipulator [38]. The elemental composition of the TEM slices was determined using an energy-dispersive X-ray spectroscopy (EDX) system.

Table 1
Peak centre positions and FWHM of CoNbZr extracted from the XRD pattern.

t nm	Peak centre °	FWHM °
1040 ± 40	44.47 ± 0.02	4.30 ± 0.04
520 ± 20	44.40 ± 0.01	4.17 ± 0.03
208 ± 8	44.38 ± 0.02	4.01 ± 0.05
104 ± 4	44.44 ± 0.05	3.75 ± 0.10
52 ± 2	44.32 ± 0.08	2.96 ± 0.05
Average	44.40 ± 0.06	3.84 ± 0.53

Table 2
Peak centre positions and FWHM of Si extracted from the XRD pattern.

t nm	Peak centre °	FWHM °	Peak centre °	FWHM °
208 ± 8	47.72 ± 0.01	0.07 ± 0.01	54.55 ± 0.01	0.09 ± 0.01
104 ± 4	47.73 ± 0.01	0.09 ± 0.01	54.57 ± 0.01	0.09 ± 0.01
52 ± 2	47.56 ± 0.01	0.07 ± 0.01	54.40 ± 0.01	0.10 ± 0.01
Average	47.67 ± 0.09	0.08 ± 0.01	54.50 ± 0.09	0.09 ± 0.01

2.3. Magnetic characterisation

Magnetic measurements were performed on the as deposited films using a DMS Model 10 Vector Vibrating Sample Magnetometer (VSM) to measure both in-plane and out-of-plane magnetic hysteresis loops. The lateral sample size was 8 mm × 8 mm. The system was calibrated using a 0.3 mm thick Ni foil with the same area and a mass of 156 mg, assuming a magnetic moment of 8.61 mAm^2 based on the mass magnetisation of Ni (55.1 $A\,m^2/kg$) [39]. The diamagnetic contributions from the sample holder and Si substrate were subtracted as a linear background signal of 0.5 µA m^2/T, obtained by fitting the high-field branches of the in-plane hysteresis loops.

For MFM analysis, a Bruker Multimode 8 atomic force microscope (AFM) was used. The AFM head was positioned between two electromagnetic coils capable of applying a field B of up to 80 mT. Olympus OMCL-AC240TS cantilevers coated with 40 nm $Co_{85}Cr_{15}$ were used to detect the stray magnetic fields of the samples [40].

3. Results and discussion

This section presents the structural and magnetic properties of the CoNbZr thin films, followed by a discussion of key hypotheses based on the observed trends.

3.1. Microstructural properties

Fig. 1 shows the XRD patterns of CoNbZr films with varying thicknesses. Broad, low-intensity peaks centred at an average angle of (44.40 ± 0.06)° were observed, with an average full-width at half-maximum (FWHM) of (3.84 ± 0.53)°, as summarised in Table 1. The broadening of these peaks is due to the scattering of X-rays in multiple directions, caused by the lack of a regular atomic lattice and a statistically dominating specific range of interatomic distances [41]. This broad peak is characteristic for an amorphous state, indicating the absence of long-range crystalline order in the CoNbZr films.

In addition to the broad peak, two distinct Bragg reflections were observed at (47.67 ± 0.09)° and (54.50 ± 0.09)° (see Table 2). These reflections are attributed to the crystalline structure of the underlying (100) Si substrate, likely induced by incident W L_β radiation originating from the X-ray source, which is equipped with a tungsten filament. These Si-related reflections are distinct from the broad peak associated with the amorphous CoNbZr films.

While the XRD data suggest an amorphous structure, they do not allow to differentiate between nanocrystalline and amorphous states. To address this, electron diffraction measurements were conducted. Fig. 2 displays the electron diffraction pattern of a CoNbZr film with a

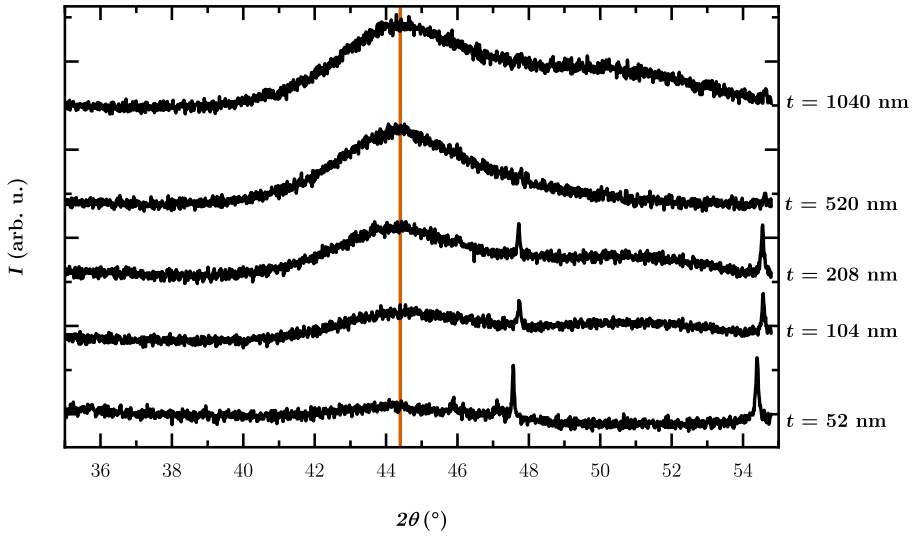

Fig. 1. XRD patterns of sputtered CoNbZr films with varying thicknesses t. The y-axis represents intensity I and the x-axis represents the diffraction angle 2θ. The broad peaks around $(44.40 \pm 0.06)°$ (red line) indicate the presence of an amorphous phase, confirming that the CoNbZr films retain their amorphous structure as thickness increases. Two distinct Bragg reflections at $(47.67 \pm 0.09)°$ and $(54.50 \pm 0.09)°$ are attributed to the crystalline structure of the underlying (100) Si substrate.

Table 3
EDX-derived elemental composition of sputtered CoNbZr films for different thicknesses.

t nm	Co at. %	Nb at. %	Zr at. %
1040 ± 40	89.5 ± 0.5	8.5 ± 0.5	1.9 ± 0.5
520 ± 20	90.5 ± 0.5	7.8 ± 0.5	1.8 ± 0.5
208 ± 8	89.3 ± 0.5	9.0 ± 0.5	1.8 ± 0.5
104 ± 4	90.3 ± 0.5	7.9 ± 0.5	1.8 ± 0.5
52 ± 2	90.2 ± 0.5	8.0 ± 0.5	1.8 ± 0.5
Average	90.0 ± 0.5	8.2 ± 0.5	1.8 ± 0.1

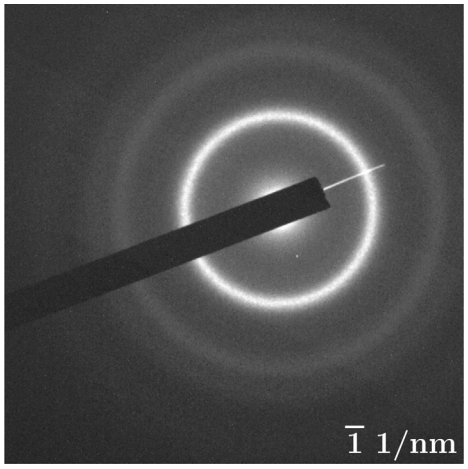

Fig. 2. Electron diffraction pattern of a sputtered CoNbZr film with a thickness of 208 nm. The presence of diffuse rings is indicative of an amorphous state.

thickness of 208 nm. The presence of diffuse rings, rather than discrete diffraction spots, is consistent with an amorphous structure, corroborating the XRD findings.

EDX analysis confirmed that all sputtered films consistently exhibit an average nominal composition of $Co_{90}Nb_8Zr_2$, as listed in Table 3, clearly deviating from the target composition ($Co_{85}Nb_{12}Zr_3$). This discrepancy is likely attributable to differences in the sputtering yields and angular distributions of the target elements, which are influenced by their respective atomic masses, binding energies, and the overall sputtering geometry [42]. In particular, the sputtering yield of Co is known to be approximately twice as high as that of Nb under comparable conditions, which can lead to an enhanced Co concentration in the resulting film [43].

These results confirm that the microstructure of the CoNbZr films remains fully amorphous across all thicknesses studied, with no evidence of crystalline growth. This structural consistency ensures that any changes in magnetic behaviour with increasing thickness can be attributed primarily to magnetic and morphological mechanisms, rather than to structural phase transitions or crystallinity effects.

3.2. Magnetic properties

Fig. 3 presents the out-of-plane hysteresis loops of amorphous CoNbZr films with varying thicknesses, measured using VSM at a maximum field sweep of $B = \pm 2$ T. Due to a slight inevitable misalignment of approximately 2° between the film plane normal and the external field direction, a small in-plane magnetisation component is observed. Between −1.4 T and −20 mT, the magnetisation decreases proportionally with the external field as it rotates toward the plane of the film. At −20 mT, the in-plane component reaches approximately −0.7 mT, nearly sufficient to saturate the films in-plane. At 20 mT, the films are saturated in-plane, and further increases in the magnetic field cause the magnetisation to rotate out-of-plane, saturating at 1.4 T. The inset magnifies the low–field region ($B = \pm 20$ mT) of the out-of-plane hysteresis loops, showing the systematic decrease of the coercive field with increasing film thickness.

The saturation magnetisation M_s was estimated from the saturation magnetic moments obtained from both the in-plane and out-of-plane loops, considering a total film area of 64 mm^2 and the thicknesses measured by TEM. The uncertainties in M_s arise from alignment errors, and the precision of the film dimensions. Additionally, the slopes of the out-of-plane loops can be used to estimate M_s by calculating their intersections with the horizontal lines extrapolated from the saturation region (as indicated by the pink lines in Fig. 3). The latter assumes that in an ideal thin film, the out-of-plane hysteresis curve is a straight line where the saturation field equals the saturation magnetisation.

Both methods yield consistent estimates for M_s, as shown in Fig. 4. The analysis demonstrates that the saturation magnetisation is independent of film thickness, with an average value of (1.01 ± 0.04) MA/m.

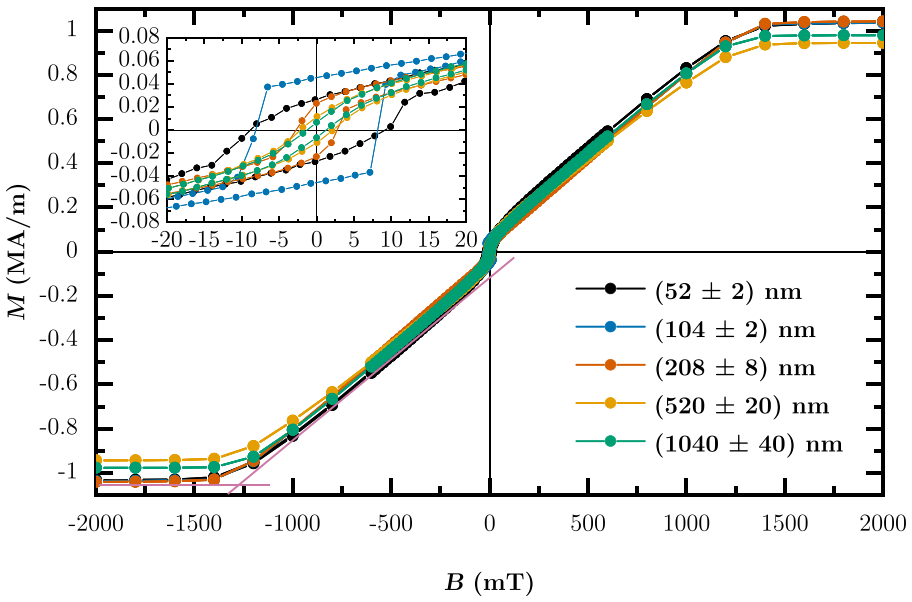

Fig. 3. Out-of-plane hysteresis loops of the magnetisation M for amorphous CoNbZr films of varying thicknesses, measured using VSM. The pink lines indicate how the saturation field was estimated. The inset magnifies the low-field region shows the systematic decrease of the coercive field with increasing film thickness.

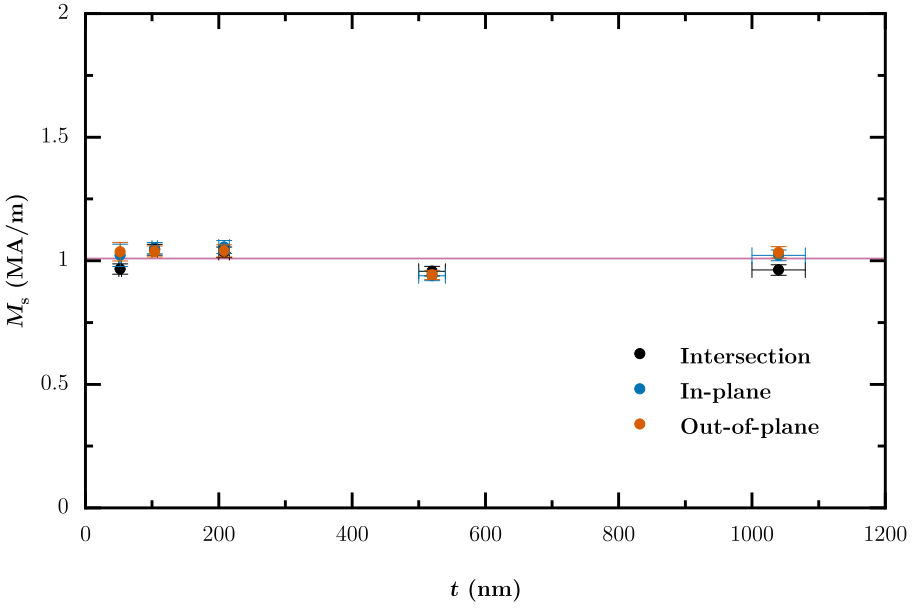

Fig. 4. Derived saturation magnetisations for various film thicknesses from the out-of-plane (black and red) and in-plane (blue) loops. The analysis shows that the saturation magnetisation is independent of film thickness (indicated by the pink line), with a mean value of (1.01 ± 0.04) MA/m.

When comparing the derived saturation magnetisation with previous studies (see Table 4), the present values are generally higher than those reported for similar CoNbZr compositions. Maximum applied fields (B_{max}) were reconstructed and, where available, film thicknesses extracted and included in Table 4. Measurements with a maximum in-plane field of 2 T ensured full magnetic saturation. As M_s is largely independent of thickness within the investigated range (see Table 4), the comparison highlights meaningful differences in saturation magnetisation while remaining primarily qualitative.

For instance, prior studies have reported M_s values of around 0.80 MA/m for $Co_{87.3}Nb_{8.8}Zr_{3.9}$ [16], 0.86 MA/m for $Co_{90}Nb_5Zr_5$ [17], and 0.88 MA/m for $Co_{85}Nb_{10}Zr_5$ [3], while values as high as 1.11 MA/m have been reported for $Co_{88}Nb_8Zr_4$ [25] and $Co_{90}Zr_{10}$ [2].

It is generally observed that a higher cobalt content results in a higher M_s, as exemplified by $M_s \approx 1.19$ MA/m for $Co_{96}Zr_4$ [2]. In contrast, increasing the Zr content tends to lower M_s [45], as does the addition of Nb [46].

To investigate how the inclusion of Nb and Zr reduces the alloy's magnetism, the saturation magnetic moment per Co atom, m_B, can be estimated using the equation $m_B = p_{Co} M_s/(\mu_B N_{Co})$, where $N_{Co} = \rho_{Co} N_A / M_{Co} \approx 9.09 \cdot 10^{-22}\,\mathrm{cm}^{-3}$ is the Co atom density, derived from the mass density ρ_{Co}, molar mass M_{Co}, and Avogadro's constant N_A. The results are summarised in Table 4. For all samples, except pure Co, the estimated magnetic moment per Co atom is significantly lower than expected. This is based on the assumption that the saturation magnetic moment per Co atom increases linearly with the Co content in the alloy, reaching a value of $m_B = 1.71\ \mu_B$/Co at 100% Co content, with a saturation magnetisation $M_s = 1.44$ MA/m [44]. The observed reduction in m_B is primarily attributed to the lack of long-range order,

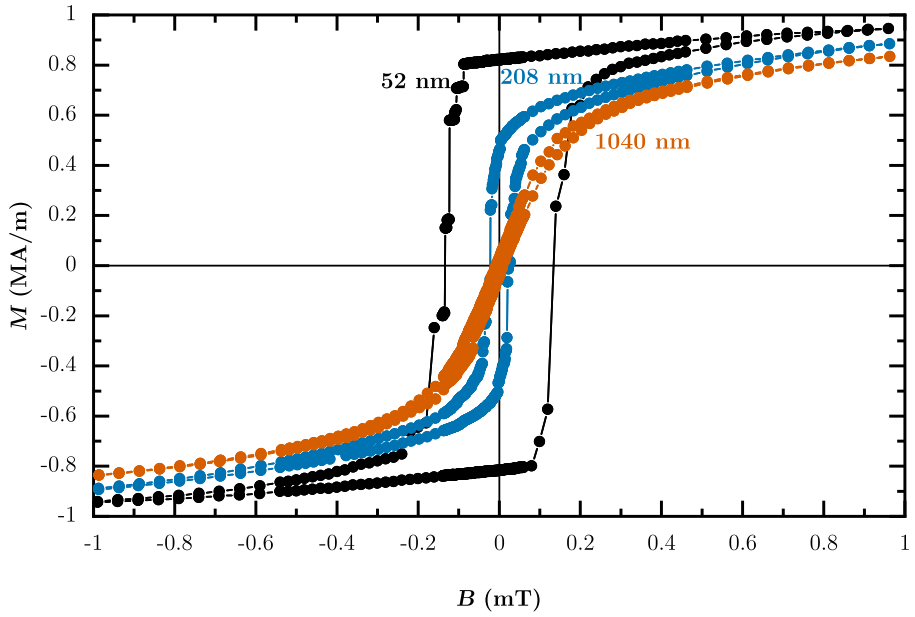

Fig. 5. In-plane hysteresis loops of the magnetisation M for amorphous CoNbZr films measured by VSM at different thicknesses. With increasing film thickness, the loop changes from a square to a smoother shape.

Table 4
Comparison of saturation magnetisations M_s with reported values, the maximum applied field B_{max}, and estimated magnetic moment per Co atom m_B. The latter is much lower than for bulk cobalt.

Composition (at.%)	t (nm)	M_s (MA/m)	m_B (μ_B/Co atom)	B_{max} (T)	Reference
Pure Co	Nanowire	1.44	1.71	>0.2	[44]
$Co_{96}Zr_4$	150–2000[a]	1.19	1.36	–	[2]
$Co_{91}Nb_7Zr_2$	52–1040	1.01	1.09	2.0	This work
$Co_{90}Zr_{10}$	150–2000[a]	0.88	0.94	–	[2]
$Co_{90}Nb_5Zr_5$	100–300[a]	0.86	0.92	>1.0	[17]
$Co_{88}Nb_8Zr_4$	1000	1.11	1.16	1.0	[25]
$Co_{87.3}Nb_{8.8}Zr_{3.9}$	1000	0.80	0.83	1.0	[16]
$Co_{85}Nb_{10}Zr_5$	2000	0.88	0.89	0.5	[3]

[a] Exact thickness t at which measurements were performed is not reported.

which weakens the exchange interactions between Co atoms, thereby reducing the overall magnetisation [46].

Fig. 5 shows the in-plane hysteresis loops of the magnetisation M recorded during a field sweep of $B = \pm 1$ mT for amorphous CoNbZr films of varying thickness. With increasing thickness, the loops evolve from a square to a more rounded shape, indicating changes in magnetic behaviour. Barkhausen jumps are observed in the thinnest film.

From these loops, the coercive field $H_c = B_c/\mu_0$, the remanent-to-saturation magnetisation ratio M_r/M_s (with M_r denoting the magnetisation at zero applied field), and the maximum slope of the magnetisation curve (maximum permeability μ_{max}) were extracted, as shown in Fig. 6. All parameters decrease with increasing film thickness: H_c from 110 A/m to 10 A/m, M_r/M_s from 0.82 to 0.05, and μ_{max} from $2 \cdot 10^5$ to $4 \cdot 10^4$. The error bars for H_c and M_r/M_s result from the inaccuracies in the interpolation of the magnetisation between field steps.

A notable observation in Fig. 6(a) and (b) is that the uncertainty of H_c and M_r/M_s decrease with increasing thickness. The increase in film thickness leads to a larger magnetic volume and consequently a higher total magnetic moment. This results in a stronger induced voltage signal in the pickup coils of the VSM, thereby improving the signal-to-noise ratio (SNR) of the measurement. Enhanced SNR reduces the relative measurement uncertainty and allows for more accurate and precise determination of H_c and M_r. Larger error bars at 52 nm thickness are attributed to Barkhausen jumps causing additional measurement uncertainties. The uncertainty in film thickness shown in Fig. 6 increases for thicker films due to the direct proportionality between thickness and deposition time. Since the deposition rate has a fixed uncertainty of ±0.2 nm/min, longer sputtering times for thicker films accumulate this uncertainty, resulting in larger absolute errors.

These findings corroborate previous studies that have also observed a decrease in coercive field with increasing film thickness [25–27]. Additionally, the coercive field at a thickness of 1040 nm is in good agreement with values reported by Shimada et al. (4 A/m [2]) and Li et al. (16 A/m [26]).

To investigate local magnetic domain structures, MFM imaging was performed on patterned 20 µm×20 µm squares with thicknesses of 52 nm and 208 nm (Fig. 7). This contrasts with the VSM measurements, which were conducted on the full 8 mm × 8 mm films to capture macroscopic magnetic properties. The thinner film exhibits an irregular domain pattern, indicating the presence of cross-tie walls (Fig. 7(a)), whereas the thicker film displays a more regular flux-closure diamond state (Fig. 7(c)). The remanent states, achieved by saturating the samples at 80 mT in-plane, show persistent irregular domains at 52 nm (Fig. 7(b)) and less regular patterns with tulip-like features at the edges at 208 nm (Fig. 7(d)).

These findings agree with the established understanding that domain wall type depends on film thickness: thinner films favour in-plane magnetisation resulting in Néel walls, while thicker films develop out-of-plane magnetisation rotation at the wall centre, leading to Bloch walls [15]. The transition thickness between Néel and Bloch walls can be approximated by $D = 20\sqrt{A/K_d}$, where A is the exchange stiffness and K_d the anisotropy constant [15]. Using literature values for the exchange stiffness $A = 11$ pJ/m [47] of Co and the experimentally measured saturation magnetisation, this transition is estimated to occur around 84 nm, in good agreement with the contrasting domain structures observed for the two thicknesses.

Although thickness-dependent domain wall transitions are well documented, for example in amorphous CoNbZr films by Wimmers and Johnson [48] and comprehensively discussed by Hubert and Schäfer [15], microstructural factors such as interface roughness, internal stresses, and multilayer architecture also play an important role in shaping domain configurations and magnetic anisotropy. Structural influences on magnetic properties have been reported in FeNi and FeNi/Ti-based

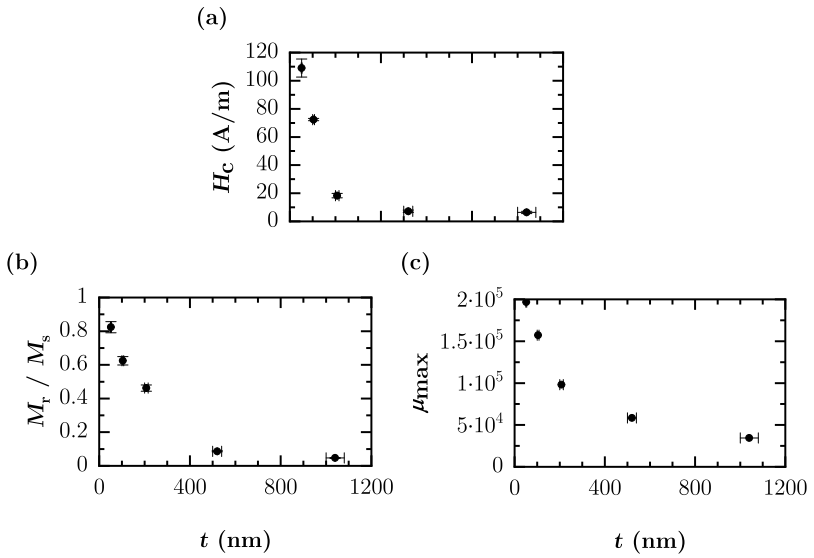

Fig. 6. Coercive field H_c, remanent-to-saturation magnetisation ratio M_r/M_s and maximum permeability number μ_{max} extracted from the in-plane hysteresis loops of amorphous CoNbZr thin films as a function of film thickness. As the film thickness increases, all the following quantities decrease: (a) H_c from 110 A/m to 10 A/m, (b) M_r/M_s from 0.82 to 0.05, and (c) μ_{max} from $2 \cdot 10^5$ to $4 \cdot 10^4$.

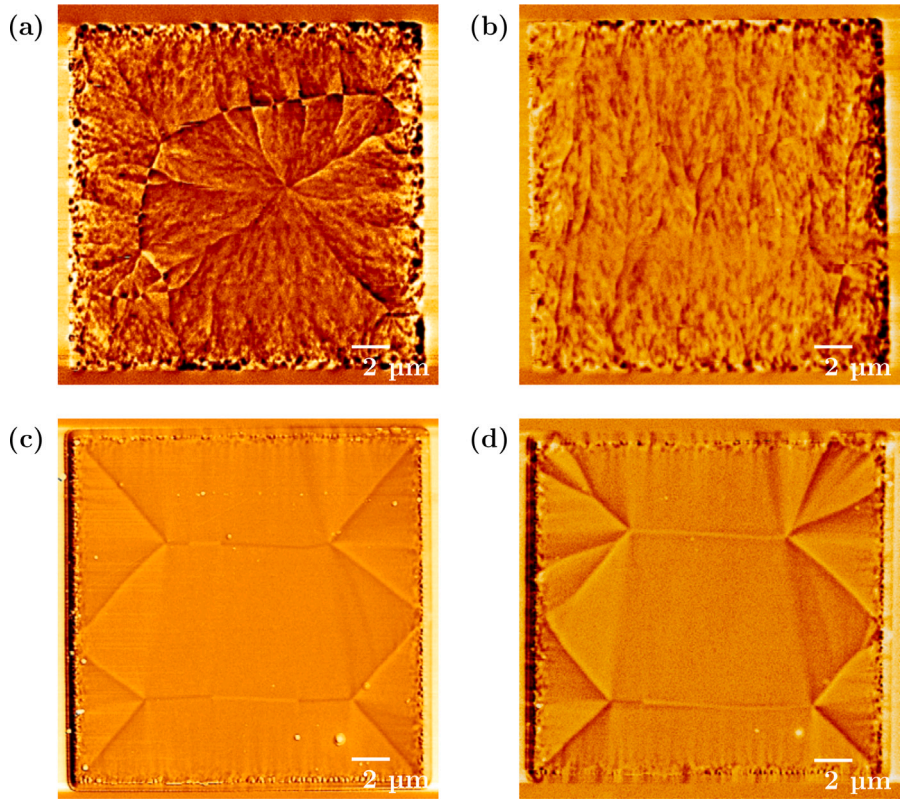

Fig. 7. MFM images of 20 µm × 20 µm patterned CoNbZr films for 52 nm (a, b) and 208 nm thickness (c, d). Hereby show (a, c) their as-prepared state and (b, d) their remanent state. The images reveal an irregular domain pattern with cross-tie walls at a thickness of 52 nm, while a regular flux-closure diamond state is observed at 208 nm in both the as-prepared and remanent states.

thin films [49], highlighting the broader relevance of combined thickness and microstructural effects for optimising CoNbZr films in sensor applications. Our results provide a direct experimental correlation between domain structures and macroscopic magnetic properties such as coercivity and permeability, which is particularly relevant for sensor performance.

3.3. Hypotheses

As evident from the hysteresis loops in Fig. 5, the remanent magnetisation state and the magnetisation reversal mechanisms vary significantly with film thickness. At an applied field of 1 mT, thinner films reach saturation more rapidly than thicker ones. This behaviour can be

attributed to the increase of the in-plane demagnetisation factors ($N_x = N_y = N$) with film thickness, reflecting the film's shape anisotropy.

The demagnetisation factors were calculated according to the analytical expressions for rectangular prisms provided by Aharoni [50], assuming uniform magnetisation (see Appendix for the full formula). These expressions neglect the material's susceptibility, which can optionally be incorporated using the correction scheme proposed by Chen et al. [51].

Using this method, the in-plane demagnetisation factors for the investigated films were determined as $N \approx 3{\cdot}10^{-5}$ for 52 nm, $N \approx 9{\cdot}10^{-5}$ for 208 nm, and $N \approx 40 \cdot 10^{-5}$ for 1040 nm. Consequently, the internal demagnetising field $\mu_0 N M_s$ increases from approximately 0.04 mT to 0.51 mT, opposing the external field. As a result, thicker films require a stronger external field to reach the same level of magnetisation.

This variation in demagnetisation field also influences the remanent magnetisation M_r, as it promotes the reorientation of magnetic domains into energetically more favourable states once the external field is removed. Similar effects have been observed in rectangular-shaped amorphous ribbons and thin films with varying geometries and anisotropies [52,53], confirming that changes in demagnetisation factors can significantly affect coercivity and permeability, which are critical parameters for sensor performance. In particular, García-Arribas et al. [54] demonstrated how tailored anisotropies in permalloy microstrips, influenced by both shape and induced effects, lead to marked variations in magnetic response.

Additionally, the observed MFM contrast in Fig. 7(b) suggests a weak perpendicular component in the magnetisation of the remanent state. This interpretation is based on the ripple-like domain pattern exhibiting alternating bright and dark contrast, which typically indicates stray fields arising from out-of-plane magnetisation components. To assess whether surface roughness contributes to this effect, the root-mean-square (RMS) roughness was evaluated from five 2 µm × 2 µm regions on each 20 µm × 20 µm MFM topography image using Gwyddion. The average RMS roughness values were (0.20 ± 0.01) nm for the 52 nm film and (0.68 ± 0.01) nm for the 208 nm film, confirming an increase of surface roughness with film thickness [55]. These low values suggest that surface morphology is unlikely to be the primary origin of the observed perpendicular anisotropy. XRD analysis further confirms that all films remain fully amorphous across the entire thickness range, excluding columnar growth or crystalline texture effects that are commonly linked to perpendicular anisotropy in sputtered films [32]. Furthermore, columnar growth, when present, is typically enhanced at greater film thicknesses, and would therefore be expected to result in a stronger out-of-plane component in thicker films. However, the MFM contrast becomes notably less pronounced in the 208 nm film compared to the 52 nm film, contradicting this expectation. Therefore, while the observed contrast may reflect a weak perpendicular anisotropy contribution, its precise microscopic origin remains unclear and requires further investigation.

4. Conclusion

As-prepared amorphous CoNbZr thin films deposited on Si-SiO_2 wafers were systematically investigated, varying in thickness from 52 nm to 1040 nm.

XRD spectra and TEM diffraction patterns confirmed that the CoNbZr films maintain their amorphous structure across all thicknesses. EDX analyses indicated consistent stoichiometry in the sputtered films, with compositions of $Co_{90\pm1}Nb_{8\pm1}Zr_{2\pm1}$. The saturation magnetisation was found to be constant, with a mean value of (1.01 ± 0.04) MA/m. Based on this saturation magnetisation and the film composition, the magnetic moment per Co atom was estimated to be approximately 60% lower than that of pure cobalt.

In contrast to the saturation magnetisation, the coercive field exhibits a significant reduction with increasing film thickness, decreasing by a factor of 10 to a value of 10 A/m. Similarly, the ratio of remanent-to-saturation magnetisation decreases by a factor of 16, reaching a minimum value of 0.05. The maximum permeability number also decreases by a factor of 5 down to $4 \cdot 10^4$.

MFM measurements revealed an irregular domain pattern with cross-tie walls at a thickness of 52 nm, while 208 nm thickness has shown a regular flux-closure diamond state in both, as-deposited and saturated films. This behaviour is attributed to the transition between Néel and Bloch type domain walls, which is expected to occur at approximately 84 nm.

Although the transition from Néel to Bloch domain walls with increasing film thickness is a well-established micromagnetic phenomenon, this work extends the understanding by quantitatively linking domain wall evolution to changes in permeability, coercivity, and hysteresis behaviour in amorphous CoNbZr films produced by RF magnetron sputtering. These correlations are directly relevant for the optimisation of CoNbZr-based magnetic sensors, as high permeability and low coercivity are essential for optimal magnetic performance. The results further demonstrate that optimised CoNbZr thin films can achieve superior magnetic behaviour compared with thicker films of equivalent total thickness, offering practical guidance for the design and fabrication of high-performance thin-film magnetic sensors.

CRediT authorship contribution statement

Indujan Sivanesarajah: Writing – review & editing, Writing – original draft, Visualization, Validation, Methodology, Investigation, Formal analysis, Data curation, Conceptualization. **Leon Abelmann:** Writing – review & editing, Validation, Supervision, Resources, Methodology, Investigation, Data curation, Conceptualization. **Uwe Hartmann:** Writing – review & editing, Supervision, Resources, Project administration, Funding acquisition.

Declaration of Generative AI and AI-assisted technologies in the writing process

During the preparation of this work, the authors used ChatGPT to improve the readability, language, grammar, spelling, and style of the manuscript. After using this tool, the authors reviewed and edited the content as needed and take full responsibility for the content of the publication.

Declaration of competing interest

The authors declare that they have no known competing financial interests or personal relationships that could have appeared to influence the work reported in this paper.

Acknowledgements

The project was conducted at Saarland University as part of the BMBF-funded collaborative research initiative "ForMikro-spinGMI". We would like to thank Dr. Oliver Janka from the Service Center for X-ray Diffraction at Saarland University for his invaluable support in collecting the X-ray diffraction data used in this work. We also thank Jörg Schmauch from INM Saarbrücken for his assistance with the TEM measurements.

Further thanks go to Christoph Pauly from the Chair of Functional Materials for his work on FIB structuring and milling, Carsten Brill from KIST Europe for his assistance with film deposition, and Gregor Büttel for his valuable contributions throughout the project.

Appendix. Demagnetisation factors for rectangular prisms

This appendix provides the full analytical expression for the in-plane demagnetisation factors of rectangular prisms, which was used to calculate the numerical values reported in the main text. For the studied films, the lateral dimensions are equal ($2a = 2c$) and the thickness is $2b$. The full expression reads [50]:

$$\begin{aligned}\pi N = &\frac{b^2-c^2}{2bc}\ln\left(\frac{\sqrt{a^2+b^2+c^2}-a}{\sqrt{a^2+b^2+c^2}+a}\right)+\frac{a^2-c^2}{2ac}\ln\left(\frac{\sqrt{a^2+b^2+c^2}-b}{\sqrt{a^2+b^2+c^2}+b}\right)\\ &+\frac{b}{2c}\ln\left(\frac{\sqrt{a^2+b^2}+a}{\sqrt{a^2+b^2}-a}\right)+\frac{a}{2c}\ln\left(\frac{\sqrt{a^2+b^2}+b}{\sqrt{a^2+b^2}-b}\right)\\ &+\frac{c}{2a}\ln\left(\frac{\sqrt{b^2+c^2}-b}{\sqrt{b^2+c^2}+b}\right)+\frac{c}{2b}\ln\left(\frac{\sqrt{a^2+c^2}-a}{\sqrt{a^2+c^2}+a}\right)\\ &+2\arctan\left(\frac{ab}{c\sqrt{a^2+b^2+c^2}}\right)+\frac{a^3+b^3-2c^3}{3abc}\\ &+\frac{a^2+b^2-2c^2}{3abc}\sqrt{a^2+b^2+c^2}+\frac{c}{ab}\left(\sqrt{a^2+c^2}+\sqrt{b^2+c^2}\right)\\ &-\frac{(a^2+b^2)^{3/2}+(b^2+c^2)^{3/2}+(c^2+a^2)^{3/2}}{3abc}.\end{aligned} \tag{A.1}$$

These expressions assume uniform magnetisation and neglect the material's susceptibility. A susceptibility correction following Chen et al. [51] can optionally be applied.

Data availability

Data will be made available on request.

References

[1] K. Handrich, S. Kobe, Amorphe Ferro- Und Ferrimagnetika, Akademie-Verlag, 1980.
[2] Y. Shimada, H. Kojima, J. Appl. Phys. 53 (1982) 3156.
[3] H. Sakakima, IEEE Trans. Magn. 19 (1983) 131.
[4] G. Herzer, Acta Mater. 61 (2013) 718.
[5] T. Meydan, J. Magn. Magn. Mater. 133 (1994) 525.
[6] C.P.O. Treutler, Sensors Actuators, A: Phys. 91 (2001) 2.
[7] C. Morón, C. Cabrera, A. Morón, A. García, M. González, Sensors (Switzerland) 15 (2015) 28340.
[8] V. Korenivski, J. Magn. Magn. Mater. 215 (2000) 800.
[9] M.S. Ryłko, K.J. Hartnett, J.G. Hayes, M.G. Egan, Conf. Proc. - IEEE Appl. Power Electron. Conf. Expo. - APEC (2009) 2043.
[10] D. Gardner, G. Schrom, F. Paillet, B. Jamieson, T. Karnik, S. Borkar, IEEE Trans. Magn. 45 (2009) 4760.
[11] H.I. Hsiang, L.C. Wu, C.C. Chen, W.H. Lee, Materials 15 (2022) 1.
[12] R. Hasegawa, Mater. Sci. Eng.: A 375- 377 (2004) 90.
[13] F. Chai, Z. Li, L. Chen, Y. Pei, IEEE Trans. Magn. 57 (2020) 1.
[14] Y. Enomoto, R. Takahata, D. Satoh, Y. Marukawa, H. Sano, IEEJ J. Ind. Appl. 12 (2023) 1127.
[15] A. Hubert, R. Schäfer, Magnetic Domains, Springer Berlin Heidelberg, 2009.
[16] H.J. de Wit, C.H. Witmer, F.W. Dirne, IEEE Trans. Magn. 23 (1987) 2123.
[17] R. Zuberek, H. Szymczak, D. Zymierska, G. Suran, M. Naili, J. Magn. Magn. Mater. 104- 107 (1992) 117.
[18] Z. Marinho, S. Cardoso, R. Chaves, R. Ferreira, L.V. Melo, P.P. Freitas, J. Appl. Phys. 109 (2011) 07E521.
[19] G. He, Y. Zhang, L. Qian, G. Xiao, Q. Zhang, J.C. Santamarina, T.W. Patzek, X. Zhang, Appl. Phys. Lett. 113 (2018) 242401.
[20] F. Maspero, S. Cuccurullo, D. Mungpara, A. Schwarz, R. Bertacco, J. Magn. Magn. Mater. 535 (2021) 168072.
[21] M. Yamaguchi, M. Takezawa, H. Ohdaira, K. Arai, A. Haga, Sensors Actuators A: Phys. 81 (2000) 102.
[22] K.H. Kim, M. Yamaguchi, J. Appl. Phys. 99 (2006) 08M902.
[23] S. Yabukami, K. Kato, T. Ozawa, N. Kobayashi, K. Arai, J. Magn. Soc. Jpn. 38 (2014) 25.
[24] B. Peng, W.L. Zhang, Q.Y. Xie, W.X. Zhang, H.C. Jiang, J. Non-Cryst. Solids 365 (2013) 59.
[25] T. Takahashi, M. Yoneda, M. Naoe, Japan. J. Appl. Phys. 28 (1989) 379.
[26] X.W. Li, C. Song, J. Yang, F. Zeng, K.W. Geng, F. Pan, J. Magn. Magn. Mater. 315 (2007) 120.
[27] Y. Cao, C. Zhou, J. Magn. Magn. Mater. 324 (2012) 1832.
[28] H. Katada, T. Shimatsu, I. Watanabe, H. Muraoka, Y. Nakamura, Y. Sugita, J. Magn. Soc. Jpn. 24 (2000) 539.
[29] D. Garcia, J. Munoz, G. Kurlyandskaya, M. Vazquez, M. Ali, M. Gibbs, IEEE Trans. Magn. 34 (1998) 1153.
[30] N. Amos, R. Fernandez, R. Ikkawi, B. Lee, A. Lavrenov, A. Krichevsky, D. Litvinov, S. Khizroev, J. Appl. Phys. 103 (2008) 07E732.
[31] A.V. Svalov, I.R. Aseguinolaza, A. Garcia-Arribas, I. Orue, J.M. Barandiaran, J. Alonso, M.L. Fernández-Gubieda, G.V. Kurlyandskaya, IEEE Trans. Magn. 46 (2010) 333.
[32] S. Singh, L. Abelmann, H. Gao, U. Hartmann, J. Magn. Magn. Mater. 586 (2023) 171138.
[33] M. Yamaguchi, S. Tanaka, Y. Endo, S. Muroga, M. Nagata, Asia-Pacific International Symposium on Electromagnetic Compatibility, APEMC, Vol. 536, 2015.
[34] D. Battistel, G. Battaglin, S. Daniele, Sensors Actuators B: Chem. 191 (2014) 143.
[35] A. Chargui, R.E. Beainou, A. Mosset, S. Euphrasie, V. Potin, P. Vairac, N. Martin, Nanomaterials 10 (2020) 81.
[36] G. Elomari, H. Larhlimi, R. Oubaki, E. Elmaataouy, M. Aqil, Y. Samih, M. Makha, C. Negrila, J. Alami, M. Dahbi, J. Power Sources 642 (2025) 236967.
[37] J. Fassbender, J. McCord, J. Magn. Magn. Mater. 320 (2008) 579.
[38] D. Tomus, H.P. Ng, Micron 44 (2013) 115.
[39] J. Crangle, G.M. Goodman, Proc. R. Soc. A 321 (1971) 477.
[40] K. Babcock, V. Elings, M. Dugas, S. Loper, IEEE Trans. Magn. 30 (1994) 4503.
[41] B. Cullity, S. Stock, Elements of X-Ray Diffraction, Third ed., Pearson Education Limited, 2014.
[42] J. Neidhardt, S. Mráz, J.M. Schneider, E. Strub, W. Bohne, B. Liedke, W. Möller, C. Mitterer, J. Appl. Phys. 104 (2008) 063304.
[43] Y. Ochiai, K. Aso, M. Hayakawa, H. Matsuda, K. Hayashi, W. Ishikawa, Y. Iwasaki, J. Vac. Sci. Technol. A: Vac. Surfaces, Films 4 (1986) 19.
[44] L. Sun, Y. Hao, C.L. Chien, P.C. Searson, P.C. Searson, IBM J. Res. Dev. 49 (2005) 79.
[45] S. Ohnuma, K. Shirakawa, M. Nose, T. Masumoto, IEEE Trans. Magn. 16 (1980) 1129.
[46] A. Lekdadri, R. Chami, A. Saadi, H. Lassri, L. Omari, Mater. Today: Proc. 37 (2021) 3813.
[47] A. Yoshihara, K. Takanashi, M. Shimoda, O. Kitakami, Y. Shimada, Japan. J. Appl. Phys. 33 (1994) 3927.
[48] O. Wimmers, M. Johnson, J. Magn. Magn. Mater. 96 (1991) 97.
[49] N.V. Alzola, G.V. Kurlyandskaya, A. Larrañaga, A.V. Svalov, IEEE Trans. Magn. 48 (2012) 1605.
[50] A. Aharoni, J. Appl. Phys. 83 (1998) 3432.
[51] D.-X. Chen, E. Pardo, A. Sanchez, IEEE Trans. Magn. 41 (2005) 2077.
[52] A.A. Pasynkova, A.V. Timofeeva, V.A. Lukshina, E.A. Stepanova, G.V. Kurlyandskaya, Phys. Met. Met. 123 (2022) 746.
[53] A. Chaturvedi, T.P. Dhakal, S. Witanachchi, A.-T. Le, M.-H. Phan, H. Srikanth, Mater. Sci. Eng. B 172 (2010) 146.
[54] A. García-Arribas, E. Fernández, A.V. Svalov, G.V. Kurlyandskaya, A. Barrainkua, D. Navas, J.M. Barandiaran, Eur. Phys. J. B 86 (2013) 136.
[55] A. Rauf, Y. Fang, H. Zhang, G. Peng, T. Feng, J. Non-Cryst. Solids 521 (2019) 119500.